




Freezing-assisted preparation of self-cleaning, high-flux photocatalytic nanocomposite membranes for enhanced degradation of antibiotic activity

Minjia Meng^{1,5,*} , Jian Zheng¹, Yanhua Cui², Binrong Li³, Lili Yang¹, Yu Zhu⁴, and Chunxiang Li¹

¹Institute of Green Chemistry and Chemical Technology, School of Chemistry and Chemical Engineering, Jiangsu University, Zhenjiang 212013, China

²School of Materials Science and Engineering, Jiangsu University, Zhenjiang 212013, China

³School of Environment and Safety Engineering, Jiangsu University, Zhenjiang 212013, China

⁴College of Pharmacy and Chemistry and Chemical Engineering, Taizhou University, Taizhou 225300, People's Republic of China

⁵Jiangsu Agrochem Laboratory Co., Ltd, Chang Zhou 213022, Jiangsu, China

Received: 9 March 2021

Accepted: 9 August 2021

Published online:

3 January 2022

© The Author(s), under exclusive licence to Springer Science+Business Media, LLC, part of Springer Nature 2021

ABSTRACT

The weak light absorption capacity and the embedding of active sites are the main factors that affect the photodegradation performance of blending photocatalytic membrane. Herein, a Z-scheme $\text{TiO}_2/\text{rGO}/\text{ZnCdS}/\text{PVDF}$ photocatalytic composite membrane (T-rGO-ZCSM) with excellent mechanical properties and good self-cleaning performance was successfully prepared by the freezing phase inversion method. As the solvent turns to crystal under freezing temperature, the micron-scale ordered penetrating porous structure formed after phase inversion, which can efficiently improve the water flux ($19000\text{--}25000 \text{ L m}^{-2} \text{ h}^{-1} \text{ bar}^{-1}$) and light penetration. Meanwhile, Z-scheme $\text{TiO}_2/\text{rGO}/\text{ZnCdS}$ heterojunctions will be migrated to the surface of the large pore canal due to their hydrophilicity during the phase inversion process. This structure can promote light absorption and increase effectively contact between active sites and pollutants. The T-rGO-ZCSM also exhibits outstanding photocatalytic activity for removing the various antibiotics under visible light, such as tetracycline (TC), levofloxacin (LEV), and ciprofloxacin (CIP). After four cycles (1.0 h for each cycle) of experiments, T-rGO-ZCSM has good stability and reusability. Moreover, the TC degradation efficiency of T-rGO-ZCSM reached the highest of 87.46% under continuous 6.0 h solar irradiation. The superoxide radical ($\cdot\text{O}_2^-$) and photogenerated h^+ were the main active species for organics' degradation. In summary, the ordered penetrating

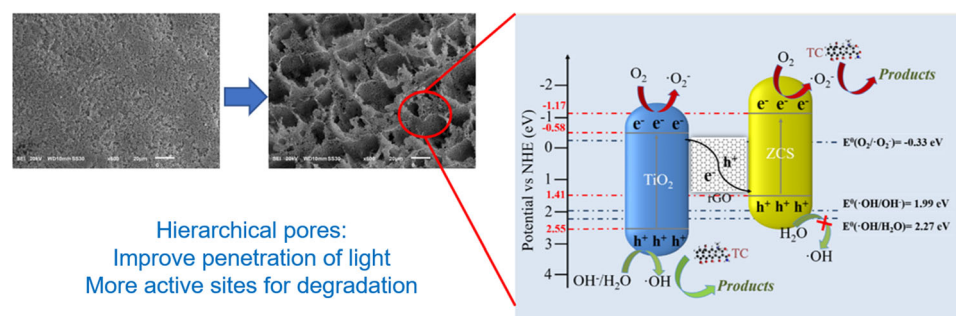
Handling Editor: Annela M. Seddon.

M. Meng and J. Zheng have contributed equally.

Address correspondence to E-mail: mmj@ujs.edu.cn

type macroporous T-rGO-ZCSM has promising potentials for wider applications in wastewater treatment.

GRAPHICAL ABSTRACT



A hierarchical-ordered penetrating-type porous T-rGO-ZCSM membrane was prepared by freezing phase inversion method. The membrane surface with large pore diameters can provide a more convenient transport pathway, and pollutants can be transferred to the active sites to increase effective contact. It can also enhance the visible light absorption to excite more photogenerated carriers and improve photocatalytic activity. Finally, the photocatalytic degradation efficiency of freezing T-rGO-ZCSM could be increased by 1.71 times compared to that of the conventional blending nf-T-rGO-ZCSM under visible light.

Introduction

With the rapid development of industry and society, the pollution of the water environment is serious problem for human health [1–3]. In particular, the pollution of antibacterial drugs dominated by the pharmaceutical industry has become a topical issue of discussion [4]. Among them, antibiotics are widely used as the most common antibacterial drugs. However, antibiotics cannot be completely degraded and will exist in water for long term, leading to the production of drug-resistant bacteria and drug-resistant genes, which seriously endanger the water ecology system [5–7]. Over the past decades, various post-treatment technologies have been widely studied in solving residual antibiotics in wastewater, such as biological treatment [8], adsorption [9], membrane separation [10] and semiconductor photocatalysis [11]. Semiconductor photocatalysis has been proved to be a promising and environmentally friendly technology due to its high efficiency, low cost,

cleanness and flexible process design in the treatment of organic pollutants [12, 13]. Up to now, multitudinous semiconductor photocatalysts have been used to treat antibiotics in wastewater, such as TiO_2 [14], ZnSnO_3 [15], $g\text{-C}_3\text{N}_4$ [16] and In_2O_3 [17]. Among them, TiO_2 has attracted great interest due to its chemical stability, non-toxicity and low cost. However, the forbidden bandwidth of TiO_2 is about 3.2 eV, which can only respond to excitation in the ultraviolet region. Besides, the rapid recombination and quenching of photogenerated carriers will also reduce the photocatalytic performance of TiO_2 [18–20]. Therefore, it is necessary to reasonably design TiO_2 composites with well-match energy band structures and interface contact to achieve high mobility and separation rate of carriers.

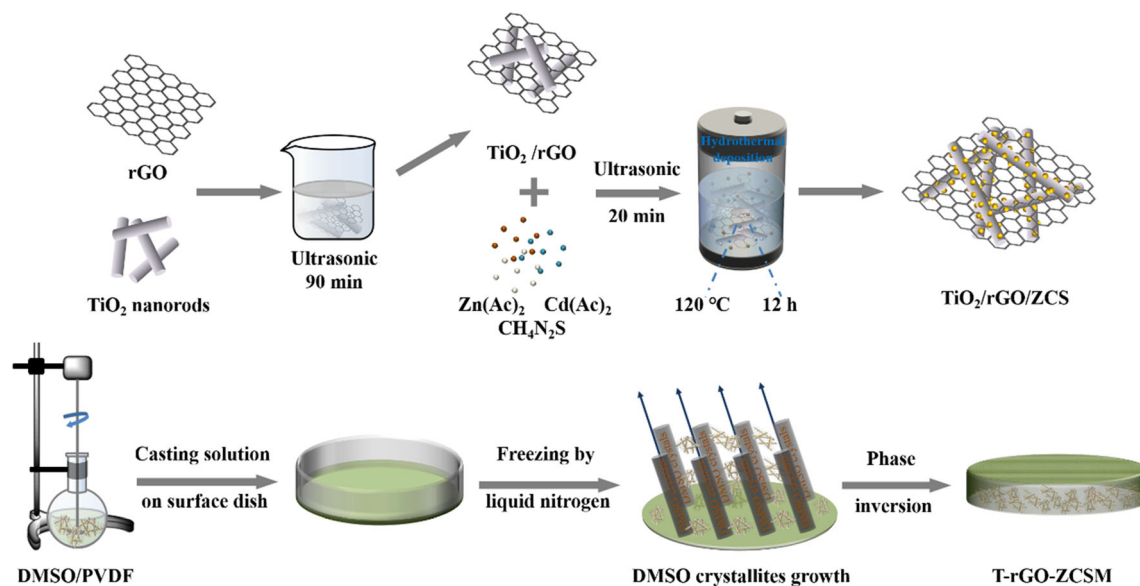
It is well known that constructing an energy band matched semiconductor Z-scheme heterostructure is an effective way to improve the photocatalytic performance of TiO_2 semiconductor material [21]. Such Z-scheme heterostructure not only broadens the visible light response range but also promotes the

separation of photogenerated electron–hole pairs through the synergistic interaction of interfaces, thereby improving the photocatalytic activity [22, 23]. As a ternary solid solution of ZnS and CdS, $Zn_xCd_{1-x}S$ has the adjustable composition and band gap width as well as a good visible light response range [24]. According to previous reports, TiO_2 and ZnCdS have suitable energy level matching [25–29]. Therefore, the preparation of Z-scheme heterojunctions by combining TiO_2 and $Zn_xCd_{1-x}S$ solid solution will be expected to improve the photocatalytic performance for the removing of organic pollutants under visible light. However, the $TiO_2/Zn_xCd_{1-x}S$ heterostructure has the disadvantages of slow separation of electron–hole pairs and sluggish surface redox kinetics [30]. Fortunately, reduced graphene oxide (rGO) has become an effective electronic medium for nanoparticles to increase the electron transport rate due to its high electron mobility, stability and excellent conductivity [31]. Besides, rGO can control the synthesis of nanoparticles and reduce agglomeration during the preparation of composite materials [32]. Therefore, the addition of rGO is expected to address the shortcomings of the $TiO_2/Zn_xCd_{1-x}S$ heterostructure.

However, the application of powdered photocatalyst in the wastewater treatment has been limited by their small particle size, susceptibility to loss and agglomeration, and difficulty in separation and recovery from treated water [33, 34]. For large-scale applications, blending the photocatalyst within the membrane is considered to be a convenient and economic modification method for recyclability in practical applications [35–38]. This not only effectively treats organic pollutants in wastewater, but also prevents membrane contamination and improves membrane permeability and membrane lifetime [39]. For instance, Hu et al. [40] successfully prepared the $Bi_2WO_6/MOF/PVDF$ composite membrane, and efficiently degraded RhB under visible light irradiation. In fact, the preparation of traditional blending photocatalytic membranes will sacrifice some active sites and light absorption capacity. Therefore, modifying the structure and morphology of the blending membrane is also an effective way to improve the photocatalytic activity [41]. As we know, adjustment of pore structure can provide a more convenient transport pathway and promote effective contact between pollutants and active sites. Moreover, the large pore diameters of membrane channel

can enhance the visible light absorption to excite more photogenerated carriers and improve photocatalytic activity [42, 43]. However, in the preparation of membranes, traditional pore-making methods usually involve the addition of organic pore-foaming reagents, but the resulting pore size is small and environmentally unfriendly, inevitably affecting catalytic performance and increasing costs [44]. Directional freezing is a low-cost and green technique to form hierarchical porous structure because it does not use any organic or inorganic additives and not involve any chemical reaction. Due to the high freezing point, dimethyl sulfoxide (DMSO) was used not only as a solvent for PVDF but also as the template. Therefore, the DMSO can rapidly and orderly form crystals under low temperature and thus many of macropores in membranes will be formed after the freezing phase inversion method [6, 45].

Inspired by the above considerations, in this work, we reported a micron-scale size ordered penetrating-type macroporous structure T-rGO-ZCSM membrane for tetracycline (TC), levofloxacin (LEV) and ciprofloxacin (CIP) degradation under visible light. A simple two-step preparation strategy was carried out as follows: (1) the Z-scheme $TiO_2/rGO/ZCS$ heterojunctions were synthesized by hydrothermal method. (2) $TiO_2/rGO/ZCS$ composite photocatalysts were blended into PVDF matrix to form photocatalytic composite membranes by freezing phase inversion method. The schematic of the synthesis procedure is illustrated in Scheme 1. Meanwhile, the structural characteristics and photocatalytic performance of $TiO_2/rGO/ZCS$ composite photocatalysts and T-rGO-ZCSM were systematically studied. Besides, the permeability, self-cleaning performance, and mechanical properties of various membranes were further studied. In general, the Z-scheme $TiO_2/rGO/ZCS$ heterojunctions can effectively improve the photocatalytic performance, and this micron-scale-size-ordered penetrating-type macroporous-structured photocatalytic membrane plays an important role in application prospects for the removal of organic pollutants.



Scheme 1 Synthesis illustration of Z-scheme $\text{TiO}_2/\text{rGO}/\text{ZCS}$ heterojunctions and T-rGO-ZCSM membranes.

Experiment

Materials

P25, graphite powder (325 mesh), 5,5-dimethyl-1-pyrroline N-oxide (DMPO, 97.0%) and vitamin C (ASC, AR) were supported from Aladdin Chemistry Co., Ltd. Absolute ethanol, sodium nitrate (NaNO_3 , 99.0%), sulfuric acid (H_2SO_4 , 98.0%), potassium permanganate (KMnO_4), hydrogen peroxide (H_2O_2 , 30.0%), hydrochloric acid (HCl , 36.0 ~ 38.0%), sodium hydroxide (NaOH , $\geq 96.0\%$), ethylene glycol ($\text{C}_2\text{H}_6\text{O}_2$, $\geq 99.5\%$), hydrazine hydrate ($\text{H}_4\text{N}_2 \cdot x\text{H}_2\text{O}$, $\geq 85.0\%$), dimethyl sulfoxide (DMSO), ethylenediaminetetraacetic acid disodium salt (EDTA-2Na, AR), isopropanol (IPA, AR), zinc acetate dihydrate ($\text{Zn}(\text{Ac})_2 \cdot 2\text{H}_2\text{O}$), cadmium acetate dihydrate ($\text{Cd}(\text{Ac})_2 \cdot 2\text{H}_2\text{O}$) and thiourea ($\text{CH}_4\text{N}_2\text{S}$) were purchased from Sinopharm Chemical Reagent Co., Ltd. (Shanghai, China). Commercial polyvinylidene fluoride (PVDF) was provided by Solvay Solexis (Changshu, China). Bovine serum albumin (BSA), tetracycline (TC), levofloxacin (LEV) and ciprofloxacin (CIP) were supported from Macklin Biochemical Co., Ltd. Liquid nitrogen was used as received. Deionized (DI) water was used in the experiments.

Fabrication of T-rGO-ZCSM photocatalytic composite membranes

The synthesis methods of rGO, TiO_2 nanorods, TiO_2/rGO and $\text{TiO}_2/\text{rGO}/\text{ZCS}$ are given in the supporting information.

The $\text{TiO}_2/\text{rGO}/\text{ZCS}/\text{PVDF}$ photocatalytic composite membranes (T-rGO-ZCSM) were prepared via the freezing phase inversion method (FPI). Firstly, $\text{TiO}_2/\text{rGO}/\text{ZCS}$ composite photocatalysts were added to DMSO, and the solution was treated by ultrasonic for 0.5 h. Then PVDF powder was dissolved in the above solution and stirred at 50°C for 6.0 h to generate the casting solution. Subsequently, the casting solution was degassed at ambient temperature for 6.0 h. Afterward, the 2.5 g of casting

Table 1 Components of as-prepared membranes

Membranes	Content (wt%)			
	DMSO	PVDF	Photocatalysts	FPI
nf-PVDF	87	13	0	No
f-PVDF	87	13	0	Yes
TM	86	13	1	Yes
T-rGOM	86	13	1	Yes
T-ZCSM	86	13	1	Yes
T-rGO-ZCSM-1	86	13	1	Yes
T-rGO-ZCSM-2	85	13	2	Yes
nf-T-rGO-ZCSM-1	86	13	1	No

solution was poured into a surface dish, which will be placed above about 5 cm of a liquid nitrogen storage tank. When the temperature down below its freezing point, the crystal nucleation and growth of DMSO will formed from bottom to up surface, and thus a penetrative macroporous structure is constructed. After freezing by putting the surface dish above a liquid nitrogen storage tank, the phase inversion was completed by putting it into distilled water. For comparison, the material compositions of the casting solution for different membranes are shown in Table 1.

Characterization

The crystal structure of the synthesized material was determined by X-ray diffraction (XRD, XRD-6100). Fourier transform infrared spectra (FT-IR) were conducted on a Nicolet Nexus 470 FT-IR. UV-Vis absorption spectra were recorded in the range of 200–800 nm using a UV-Vis diffuse reflectance spectrophotometer (DRS). The X-ray photoelectron spectroscopy (XPS) was conducted on Thermo Scientific Escalab 250Xi. The morphologies of as-prepared materials were investigated by scanning electron microscope (SEM, JSM-6010 PLUS/LA) and transmission electron microscopes (TEM, JEM-2100 JEOL). The cross-sectional structure and EDS mapping of membranes were investigated by SEM JEM-6700F. The mechanical properties of membranes were carried out by WJ-LL-200 tensile testing machine. The thicknesses of membranes were measured by an electronic digital micrometer (ES NSCING). The water contact angles (WCAs) of the samples were measured by an OSA60 (LAUDA Scientific). To study the reaction mechanism, the electron spin resonance (ESR) was performed on a JESFA200 spectrometer.

The catalytic property of photocatalytic membranes

The TC, LEV and CIP were selected as the target pollutant to evaluate the photocatalytic performance of membranes under visible light irradiation (300 W Xe lamp) with wavelength cutoff filter ($\lambda \leq 420$ nm) used as the light source. Typically, a piece of the membrane was added into a beaker containing a target pollutant solution. Before irradiation, the suspension was stirred in dark for 40 min to achieve the adsorptive equilibrium between the sample and the

pollutant solution. Then 3.0 mL of the analytical solution was taken out at 10-min intervals under visible light irradiation and analyzed on the UV-Vis spectrophotometer (Cary 8454). After each reaction, the membrane was collected, washed with water many times, and dried for cyclic utilization in the next experiment. Similarly, powder catalysts were added in TC aqueous solution to study photocatalytic activities.

Trapping experiments were carried out in a TC degradation experiment similar to the previous one. Different scavengers (1 mM) were added into the target pollutant solution to trap superoxide free radical ($\cdot\text{O}_2^-$), holes (h^+) and hydroxyl radicals ($\cdot\text{OH}$).

Typically, the degradation efficiency data were fitted to the first-order kinetics model via the following equation.

$$\ln(C_0/C_t) = kt \quad (1)$$

where C_0 is feed solution and C_t and k are concentrations of TC and rate constant at the time t , respectively.

Water flux and fouling resistance

The pure water flux was calculated under the 0.8 bar for 110 min in the filtration device and recording the time. The effective volume of each record is 100 mL, and the effective area of membranes was 12.56 cm², and all the experiments were carried out in triplicate. The pure water flux (J) was calculated by the following equation.

$$J = \frac{V}{A \times \Delta t \times \Delta P} \quad (2)$$

Here, V (L) is the volume of permeate water, A (m²) is the working effective area of membranes, Δt is the filtration time, and ΔP (bar) is the filtration pressure.

The antifouling properties of the membranes were evaluated by a static protein (BSA) adsorption test. For the experiment, a piece of each membrane was immersed in a BSA solution (0.5 g/L) for 24 h to establish adsorption–elution equilibrium at room temperature. The initial and final concentration of BSA solution was measured using a UV-Vis spectrophotometry at a wavelength of 280 nm. The BSA adsorption capacity (Q) was calculated by the following equation.

$$Q = \frac{(C_0 - C) \times V}{S} \tag{3}$$

where C_0 and C are the initial and final concentrations the BSA solution, respectively. V (mL) is the volume of BSA solution and S (cm²) is the effective adsorption area of a piece of each membrane.

The membrane porosity (ϵ) was determined according to gravimetric method reported elsewhere. Briefly, a piece of wet membrane was wiped using tissue paper to remove excess water from the surface and weighed. Then dried at 50 °C to constant weight the porosity was calculated by the following equation.

$$\epsilon = \frac{\frac{W_w - W_d}{\rho_w} + \frac{W_d}{\rho_p}}{\frac{W_w - W_d}{\rho_w}} \tag{4}$$

where W_w and W_d are the weight of wet and dry membranes, respectively. ρ_w and ρ_p are the density of water (0.998 g cm⁻³) and polymer (1.785 g cm⁻³), respectively.

The mean pore radius (r) of the membranes was calculated by the Guerout-Elford-Ferry equation.

$$r = \sqrt{\frac{(2.9 - 1.7\epsilon) \times 8\eta l q}{\epsilon \times A \times \Delta P}} \tag{5}$$

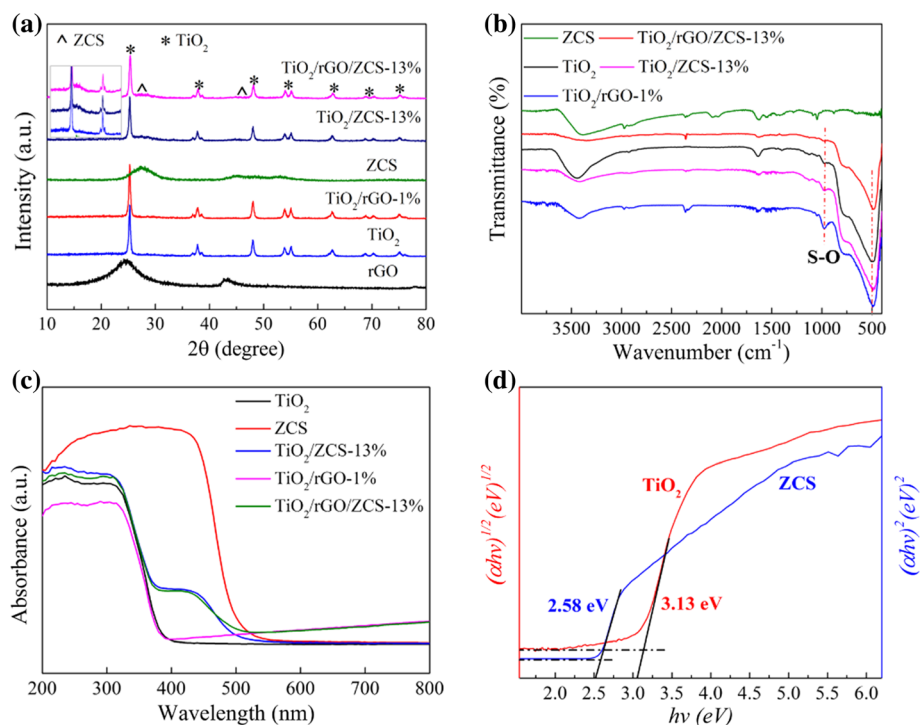
where η is the water viscosity (8.9 × 10⁻⁴ Pa s), l is the thickness of membranes (m), q is the volume of permeated water in unit time (m³ s⁻¹), A (m²) is the effective filtration area, and ΔP is the filtration pressure (Pa).

Results and discussion

Characteristics of photocatalysts

The crystal phase structures of photocatalysts were characterized by XRD. As shown in Fig. 1a, the diffraction peaks of the synthesized TiO₂ nanorods at 25.35°, 37.84°, 48.14°, 53.97°, 55.18°, 62.81°, 68.87°, 70.45°, and 75.20°, which can be assigned to the (101), (004), (200), (105), (211), (204), (116), (220), and (215) crystal planes of crystallized anatase TiO₂ (PDF#89-4921), respectively. The diffraction peak of pure Zn_{0.5}Cd_{0.5}S nanoparticles is the characteristic of Zn_{0.5}Cd_{0.5}S solid solution with sphalerite phase structure. As shown in Fig. S1, the diffraction peaks of Zn_{0.5}Cd_{0.5}S nanoparticles move to a higher-angle compared to the cubic CdS and lower-angle with respect to cubic ZnS, which indicates that the synthesized Zn_{0.5}Cd_{0.5}S is a solid solution. The characteristic peak at 26.50°, 45.10° and 53.04° can be

Figure 1 a XRD patterns, b FT-IR spectra and c UV-Vis diffuses reflectance spectra (DRS) of different samples. d Plots of $(ah\nu)^{1/2, 2}$ versus $(h\nu)$ of TiO₂ and ZCS sample.



attributed to the (111) (220), and (311) plane of $Zn_{0.5}Cd_{0.5}S$ solid solution, respectively [46]. The $TiO_2/rGO/ZCS$ -13% composite photocatalysts showed the major characteristic peaks of TiO_2 nanorods and ZCS solid solution, but the intensity of characteristic peaks of rGO was hardly observed due to their low loading amount. The above results proved the successful preparation of The $TiO_2/rGO/ZCS$ -13% composites.

The functional groups of materials were conducted to analyze using FT-IR; as shown in Fig. 1b, the main peak in the range of $450\text{--}500\text{ cm}^{-1}$ can be attributed to Ti–O–Ti and Ti–O tensile vibration modes. The peak at about 973 cm^{-1} is assigned to the symmetric tensile vibration of the S–O bond on sulfated TiO_2 nanorods [47]. For $TiO_2/rGO/ZCS$ -13% composite photocatalysts, the characteristic peak of ZCS could not be detected, which could be attributed to the low content of ZCS in inorganic nanoparticles. The other two peaks are located at 1650 and $3400\text{--}3500\text{ cm}^{-1}$, which are attributed to hydroxyl groups and absorbed water.

The optical properties of various materials were separately detected by DRS. In Fig. 1c, the wavelength of the TiO_2 adsorption edge was located at around 390 nm , which was in accordance with the intrinsic absorption of anatase TiO_2 . ZCS shows an absorption edge around 550 nm , which corresponds to its characteristic. $TiO_2/rGO/ZCS$ -13% composite

photocatalysts have a wide visible light absorption, showing an absorption edge around 520 nm . Furthermore, the $TiO_2/rGO/ZCS$ -13% sample exhibits the other one absorption in the range of $520\text{--}800\text{ nm}$ as a result of the introduction of rGO. Therefore, the secondary and wider absorption region of $TiO_2/rGO/ZCS$ -13% can make more effective use of visible light and generate more charge carriers. According to the Kubelka–Munk function, as shown in Fig. 1d, the relationship between $(\alpha hv)^{1/2}$ and the photon energy (hv) is obtained [48]. The bandgap energies of TiO_2 nanorods and ZCS are ≈ 3.13 and $\approx 2.58\text{ eV}$, respectively.

Scanning electron microscopy (SEM) and transmission electron microscopy (TEM) were used to study the morphology and microstructure of the obtained materials. In Fig. 2a, the ZCS nanoparticles synthesized tend to agglomerate together by the hydrothermal method. As displayed in Fig. 2b, d, the morphology of pure TiO_2 is irregular nanorods with a relatively smooth surface and specific surface area of $42.252\text{ m}^2\text{ g}^{-1}$ (Fig. S3a). It can be distinctly seen from Fig. 2c and e that the surface of $TiO_2/rGO/ZCS$ -13% composite photocatalysts was rough due to the ZCS nanoparticles are dispersed on the surface of TiO_2 nanorods. According to TEM images, we can ascertain the specific connection mode between TiO_2 nanorods and ZCS nanoparticles; as it is clear, ZCS nanoparticles were deposited on the surface of TiO_2

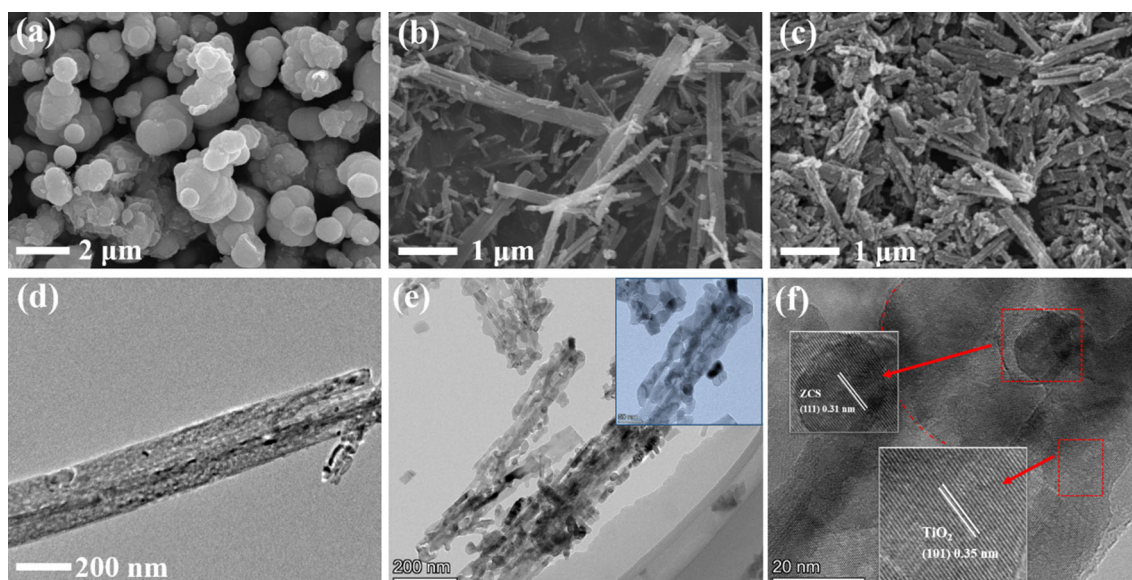


Figure 2 SEM images of **a** pure ZCS, **b** pure TiO_2 and **c** $TiO_2/rGO/ZCS$ -13%, TEM images of **d** pure TiO_2 and **e** $TiO_2/rGO/ZCS$ -13% (inset is high magnification), **f** HRTEM image of $TiO_2/rGO/ZCS$ -13%.

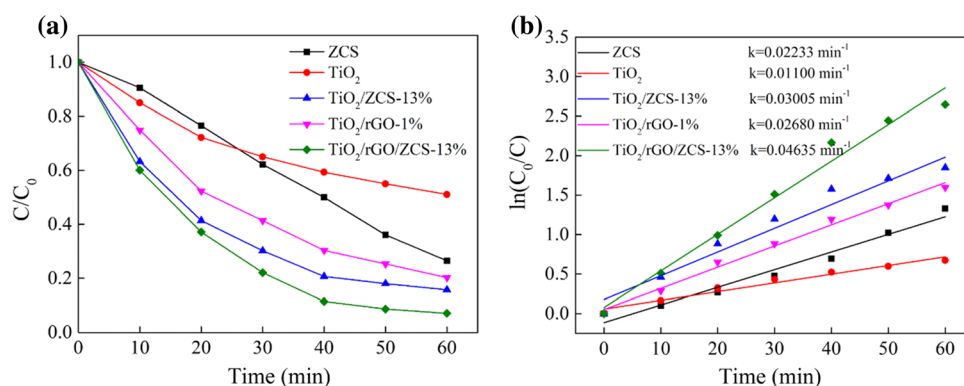
nanorods. The HRTEM image (Fig. 2f) of TiO₂/rGO/ZCS-13% can be observed that the lattice fringe spacing of TiO₂ and ZCS is 0.35 nm and 0.31 nm, which correspond to the (101) and (111) crystal plane of TiO₂ and ZCS, respectively. Meanwhile, Fig. S2 shows SEM images of TiO₂/rGO and TiO₂/ZCS, and TEM images of rGO and TiO₂/ZCS, respectively. Figure S3 shows the nitrogen adsorption–desorption isotherms of the samples. According to the classification, all photocatalysts belong to the type IV isotherms. As compared to the TiO₂/ZCS-13% ($S_{\text{BET}} = 62.258 \text{ m}^2 \text{ g}^{-1}$), the decrease in the specific surface area of TiO₂/rGO/ZCS-13% ($S_{\text{BET}} = 50.053 \text{ m}^2 \text{ g}^{-1}$) is due to the combination of rGO which blocks the pores of TiO₂ and regulates the growth of ZCS crystal nuclei (Fig. S3c and d). Barrett–Joyner–Halenda (BJH) pore size distributions of the four samples are shown in Fig. S3e, and the pore size distribution curve of TiO₂/rGO/ZCS-13% shows that there are mesopores and some micropores. This implies that a relatively high specific surface area and pore structure are important factors to improve adsorption performance and diffusion of reactants and products.

TC photodegradation performance of different photocatalysts under visible light is shown in Fig. 3. The suspension solution of TC and photocatalysts was stirred in the dark for 40 min to achieve adsorption–desorption balance before visible light irradiation. As can be observed from Fig. 3a, the TC photocatalytic degradation efficiency of the TiO₂/rGO/ZCS-13% heterojunction was the highest over the 60 min consecutive irradiation, which is 92.90%. The photocatalytic degradation efficiency of TC is only 84.24% for the TiO₂/ZCS-13% heterojunctions, which suggests that the rGO was introduced to composite, and the Z-scheme TiO₂/rGO/ZCS can

greatly enhance photocatalytic performance. The main reason is that rGO can promote the separation of photogenerated electron–hole pairs and accelerate the electron transfer. In addition, the reaction kinetics of TiO₂/rGO/ZCS-13% degradation TC was further studied by the model of $\ln(C_0/C) = kt$. As shown in Fig. 3b, compared with the TiO₂, ZCS, TiO₂/rGO-1% and TiO₂/ZCS-13%, the TiO₂/rGO/ZCS-13% (0.04635 min^{-1}) heterojunctions exhibit the higher k (apparent reaction rate constant) value about 4.21-fold, 2.07-fold, 1.73-fold and 1.54-fold as high as that of TiO₂ (0.01100 min^{-1}), ZCS (0.02233 min^{-1}), TiO₂/rGO-1% (0.02680 min^{-1}) and TiO₂/ZCS-13% (0.03005 min^{-1}), respectively. Moreover, as shown in Fig. S4, we also studied the effects of different ZCS and rGO contents on the photocatalytic performance of TC degradation. The experimental results show that the Z-scheme TiO₂/ZCS heterojunction can greatly improve the photocatalytic performance. Meanwhile, over-loaded ZCS may act as the recombination center of carriers, which inhibits the photocatalytic activity of TiO₂/ZCS heterojunction. Furthermore, although rGO is beneficial to charge transport, excessive rGO will cover the active sites of photocatalytic semiconductors and reduce the contact area between pollutants and photocatalysts.

The surface chemical structure composition of as-prepared samples is further analyzed by the X-ray photoelectron spectroscopy (XPS) in Fig. 4. Figure S5a shows the survey spectrum of the TiO₂, ZCS and TiO₂/rGO/ZCS-13%, which proves the co-existence of C, O, Ti, Zn, Cd and S elements as expected in TiO₂/rGO/ZCS-13%. Figure 4a presents the high-resolution XPS spectra of C 1s, the three peaks at 288.45, 285.99 and 284.53 eV for several carbon species with different binding energies can be attributed to C=O–C, C–O–C and C–C/C=C bonds in the

Figure 3 **a** Photocatalytic degradation rate of TC (20 mg/L) for different photocatalysts under visible light, **b** photodegradation kinetics plots of TC.



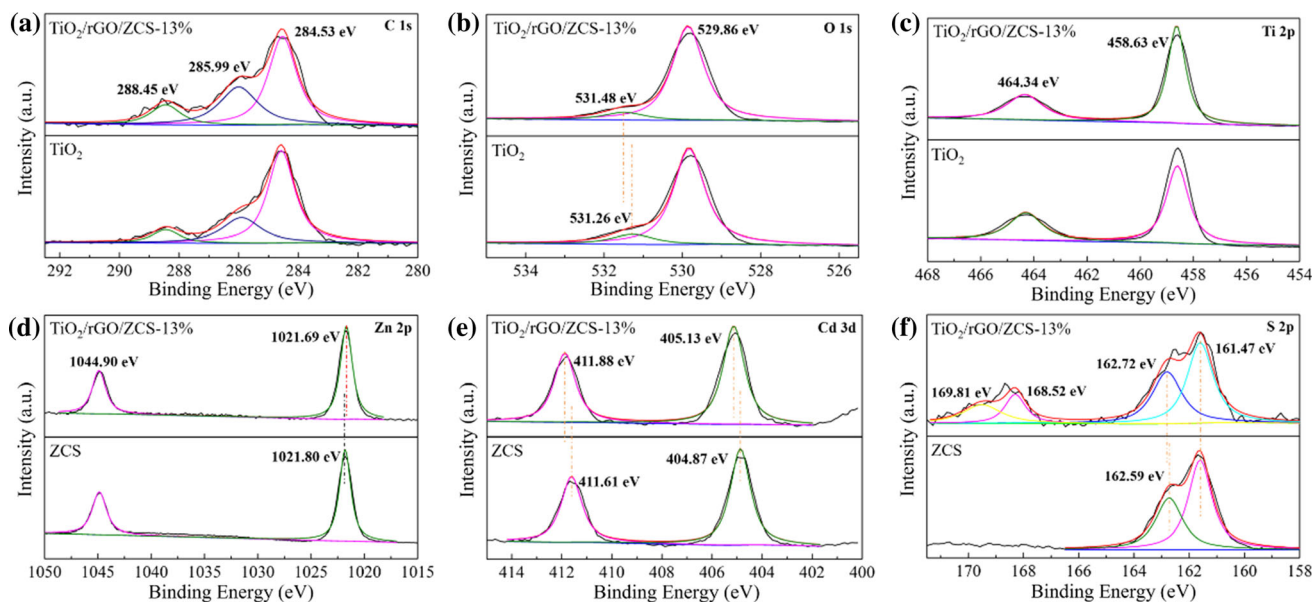


Figure 4 XPS spectra of TiO_2 , ZCS and $\text{TiO}_2/\text{rGO}/\text{ZCS}-13\%$: **a** C 1s, **b** O 1s, **c** Ti 2p, **d** Zn 2p, **e** Cd 3d and **f** S 2p.

skeleton, respectively. In $\text{TiO}_2/\text{rGO}/\text{ZCS}-13\%$, the signals of C=O–C and C–O–C increased obviously, indicating that the rGO has been successfully loaded in the catalyst. The O 1s XPS spectra are shown in Fig. 4b, and the peaks located at 531.48 and 529.86 eV are attributed to Ti–OH and Ti–O–Ti, respectively. In Fig. 4c, the two fitting peaks located at 464.34 and 458.63 eV in the characteristic binding energies for Ti 2p orbitals correspond to the Ti 2p_{1/2} and Ti 2p_{3/2}, and the 4+ oxidation state of Ti was confirmed. As shown in Fig. 4d, because Zn 2p is spin–orbit coupling, the two characteristic peaks at 1044.90 and 1021.69 eV attributed to Zn 2p_{1/2} and Zn 2p_{3/2}, respectively. Figure 4e shows Cd 3d high-resolution spectra, the main binding energy peaks are located at 411.88 eV (Cd 3d_{3/2}) and 405.13 eV (Cd 3d_{5/2}), the peak at 405.13 eV is assigned to Cd–S bond, and compared with ZCS, the binding energy of Cd 3d_{3/2} and Cd 3d_{5/2} of the $\text{TiO}_2/\text{rGO}/\text{ZCS}-13\%$ sample shifted slightly to the high binding energy region. Similarly, as shown in Fig. 4f, the binding energies at 162.72 (162.59) and 161.47 eV are attributed to the S 2p_{1/2} and S 2p_{3/2} high-resolution XPS signals, which indicates that S exists in the form of S²⁻. In $\text{TiO}_2/\text{rGO}/\text{ZCS}-13\%$ samples, the binding energy at 168.52 eV and 169.81 eV can be attributed to the sulfated TiO_2 nanorods. In the XPS test results, the opposite changes in the binding energies of each element indicate that there is intimate interfacial contact between TiO_2 nanorods, rGO and ZCS

nanoparticles, which promotes the electron transfer in $\text{TiO}_2/\text{rGO}/\text{ZCS}$ heterojunctions.

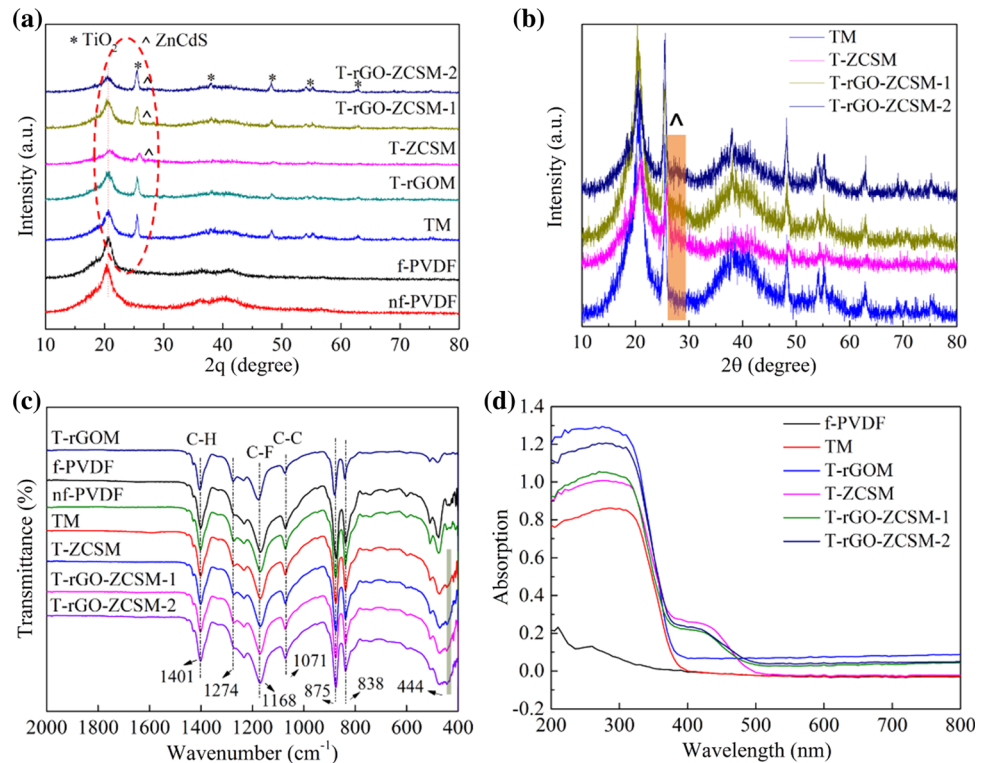
Characteristics of membranes

Figure 5a, b shows the XRD patterns of the membranes. The XRD pattern of freezing PVDF membrane shows diffraction peaks at 20.60°, 36.51° and 41.01°, indicating that PVDF is β -phase [49]. After the addition of photocatalysts, T-rGO-ZCSM showed the characteristic peaks of TiO_2 and ZCS, which correspond to the powder XRD test results. Meanwhile, the characteristic diffraction peaks at 37.84° of TiO_2 and 36.51° of freezing PVDF overlap to some extent.

The functional groups in the membranes were analyzed by FT-IR spectrogram; as shown in Fig. 5c, the absorption bands at 838, 875 and 1274 cm^{-1} attributed to the characteristic spectrum of β -phase PVDF. The peaks at 1071 cm^{-1} and 1168 cm^{-1} are indexed to the stretching vibration of C–C and –CF₂, respectively. The peaks at 1401 cm^{-1} corresponded to the deformation vibration of –CH₂ [50]. For the T-rGO-ZCSM membrane, the peaks at around 444 cm^{-1} can correspond to the vibration bands of Ti–O groups. Because the content of photocatalysts in the hybrid membrane is much lower than that of PVDF, the band intensity in the characteristic regions is weakened.

UV–Vis DRS was performed to analyze the optical property of the membranes. In Fig. 5d, the f-PVDF

Figure 5 a, b XRD patterns, c FT-IR spectra and d UV-Vis diffuses reflectance spectra (DRS) of various membranes.

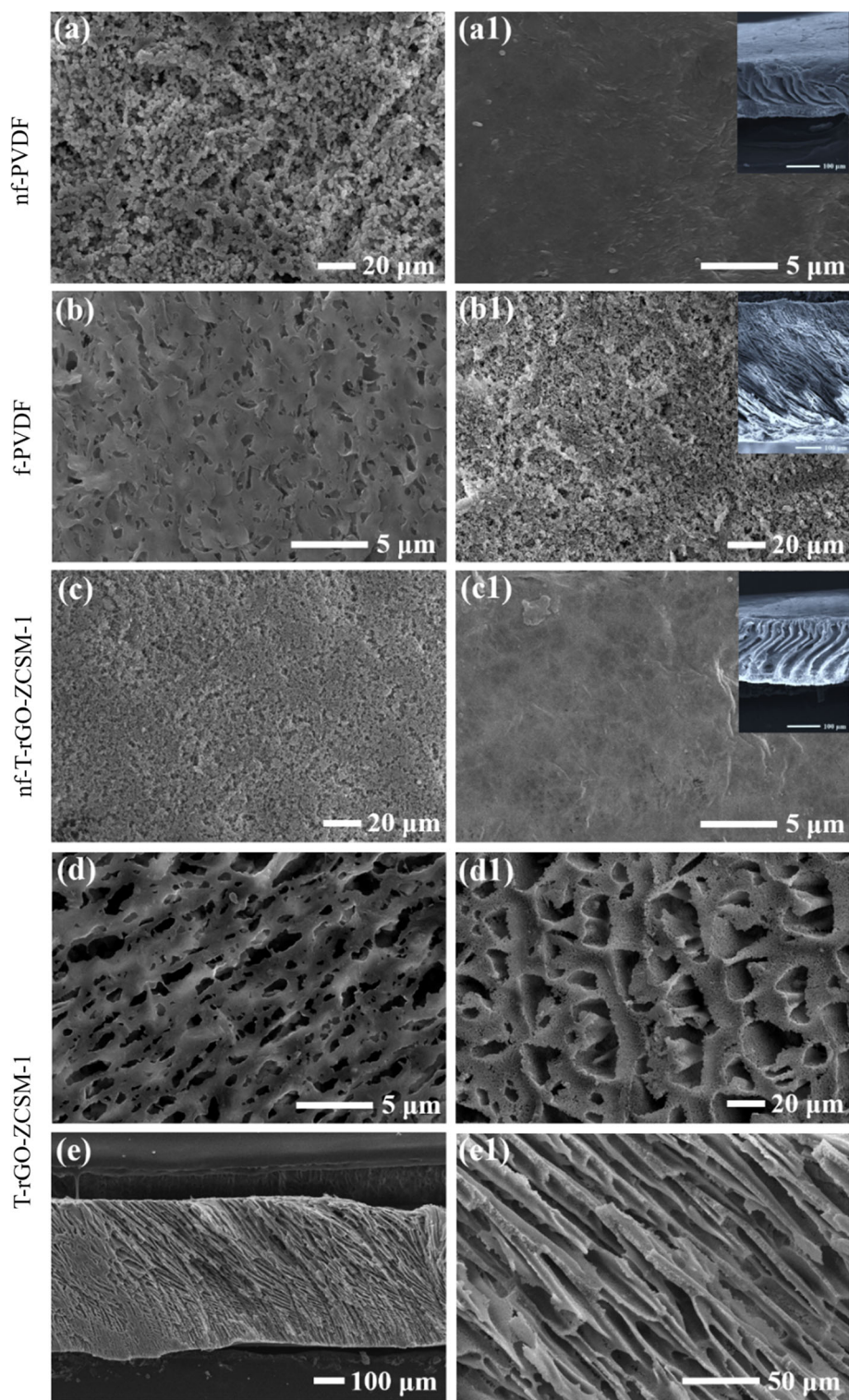


membrane shows weak light absorption intensity within 350 nm. It is worth noting that the T-rGO-ZCSM membrane owns the light absorption range of TiO₂/rGO and ZCS, but the absorption intensity is slightly reduced. Compared with the pure TiO₂ membrane, the light absorption edge of the T-rGO-ZCSM composite membrane has a slight redshift, and the absorption edge is also affected by the catalyst content in the membrane. The excellent light absorption range means that light induces more carriers and improves photocatalytic performance.

The bottom surface, top surface and cross-section morphologies of membranes were further characterized by SEM. In Fig. 6, non-freezing PVDF (nf-PVDF) and T-rGO-ZCSM (nf-T-rGO-ZCSM) have similar bottom and top surface morphology. The bottom surface of the two membranes is relatively rough, while the top surface is dense, and neither shows a pore structure. However, both the bottom and top surfaces of the freezing PVDF membrane are rough, and a small number of pore structures appear in the bottom morphology. It is worth noting that it can be seen from Fig. 6d–e1, Table 2 and Fig. S6, we can find the freezing T-rGO-ZCSM photocatalytic composite membrane shows a porous surface structure with a mean top surface pore radius of 11.014 ~ 16.821 μm.

Moreover, it can be seen from the cross-sectional view that there is a micron-scale-size-ordered penetrating-type macroporous structure in the membrane, which is caused by the rapid formation and phase transformation of DMSO crystal after freezing. The porous and macroporous structures can make full use of light sources. The light source can reflect in the large channel countless times to stimulate more photogenerated carriers and further improve the photodegradation efficiency. Among them, the porosity of the freezing membrane decreases slightly, while the mean pore radius increases exponentially, which are also attributed to the formation of the macroporous structure after freezing. With the increase in TiO₂/rGO/ZCS-13% content, the porosity of the membrane decreased from 83.17 to 80.87%, and this may be attributed to the rheological barrier caused by the increase of TiO₂/rGO/ZCS-13% content, which inhibits the exchange of DMSO with water. We also found that when rGO exists, the top surface of the membrane would form through-holes. This may be due to the rapid traction of hydrophilic particles during the freezing phase transformation process, which increases the exchange rate of solvent and water. In cross-sectional SEM images (Fig. S5), ordered penetrating-type macroporous structure was

Figure 6 a–d Bottom surface and a1–d1 top surface SEM images of membranes, e, e1 cross-section SEM images of T-rGO-ZCSM-1 membrane (insets are cross-section SEM images of the corresponding membrane, Scale bar: 100 μm).



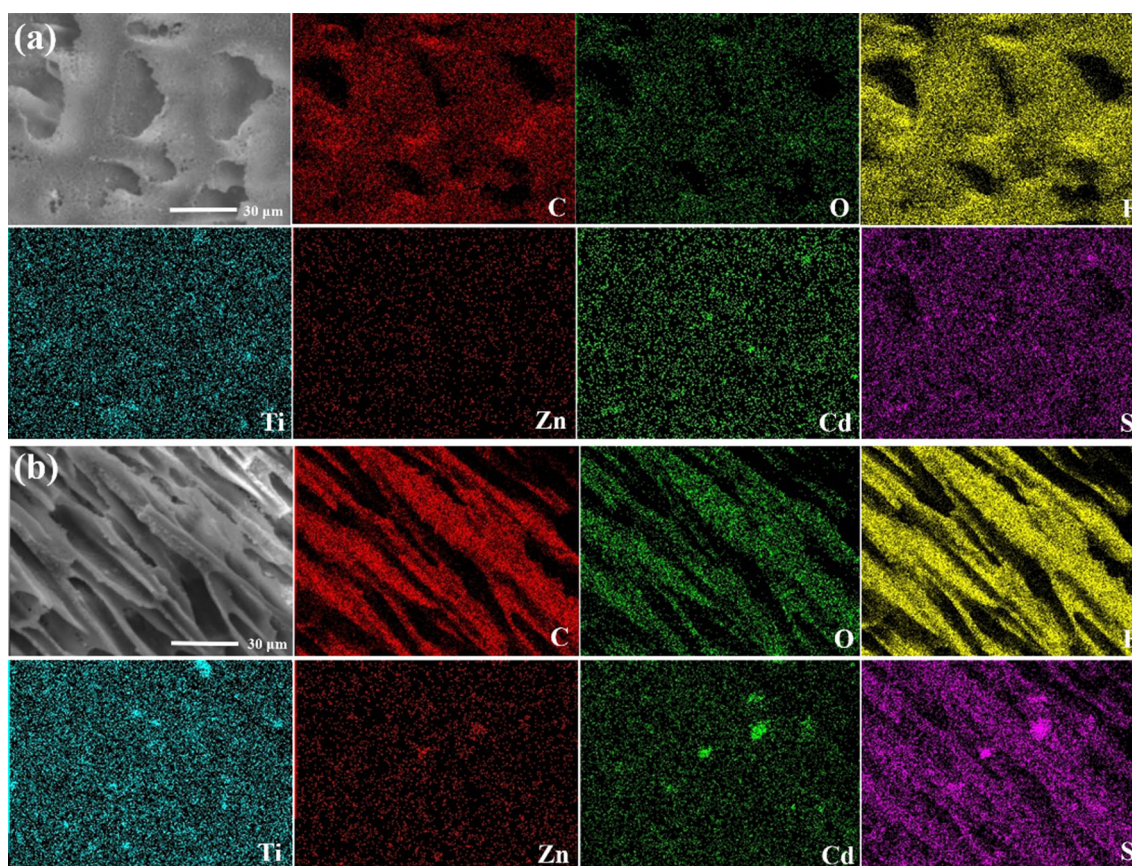
not found in non-freezing nf-PVDF and nf-T-rGO-ZCSM. Moreover, the membrane has a very thick skin layer, which will lead to the obstruction of water molecule mass transfer.

In order to study the compatibility between the inorganic catalyst and PVDF polymer matrix, the dispersion of $\text{TiO}_2/\text{rGO}/\text{ZCS}$ -13% composite photocatalysts in the membrane matrix was evaluated by EDS mapping. As can be observed from Fig. 7,

Table 2 The porosity, mean pore radius, mean surface pore radius and thickness of membranes

Membranes	Porosity (%)	Mean pore radius (um)	Mean surface pore radius (um)*	Thickness (um)
nf-PVDF	87.16	0.0376	/	0.221 ± 0.016
f-PVDF	83.72	0.8286	/	0.758 ± 0.038
TM	82.15	1.0171	/	0.773 ± 0.040
T-rGOM	80.70	0.9419	23.90 ± 2.010	0.671 ± 0.031
T-ZCSM	80.55	0.9704	/	0.656 ± 0.022
T-rGO-ZCSM-1	83.17	0.9099	12.44 ± 1.426	0.801 ± 0.021
T-rGO-ZCSM-2	80.87	0.7258	15.38 ± 1.441	0.676 ± 0.024
nf-T-rGO-ZCSM-1	86.37	0.0367	/	0.220 ± 0.019

*Data were obtained according to SEM image analysis using Image J software

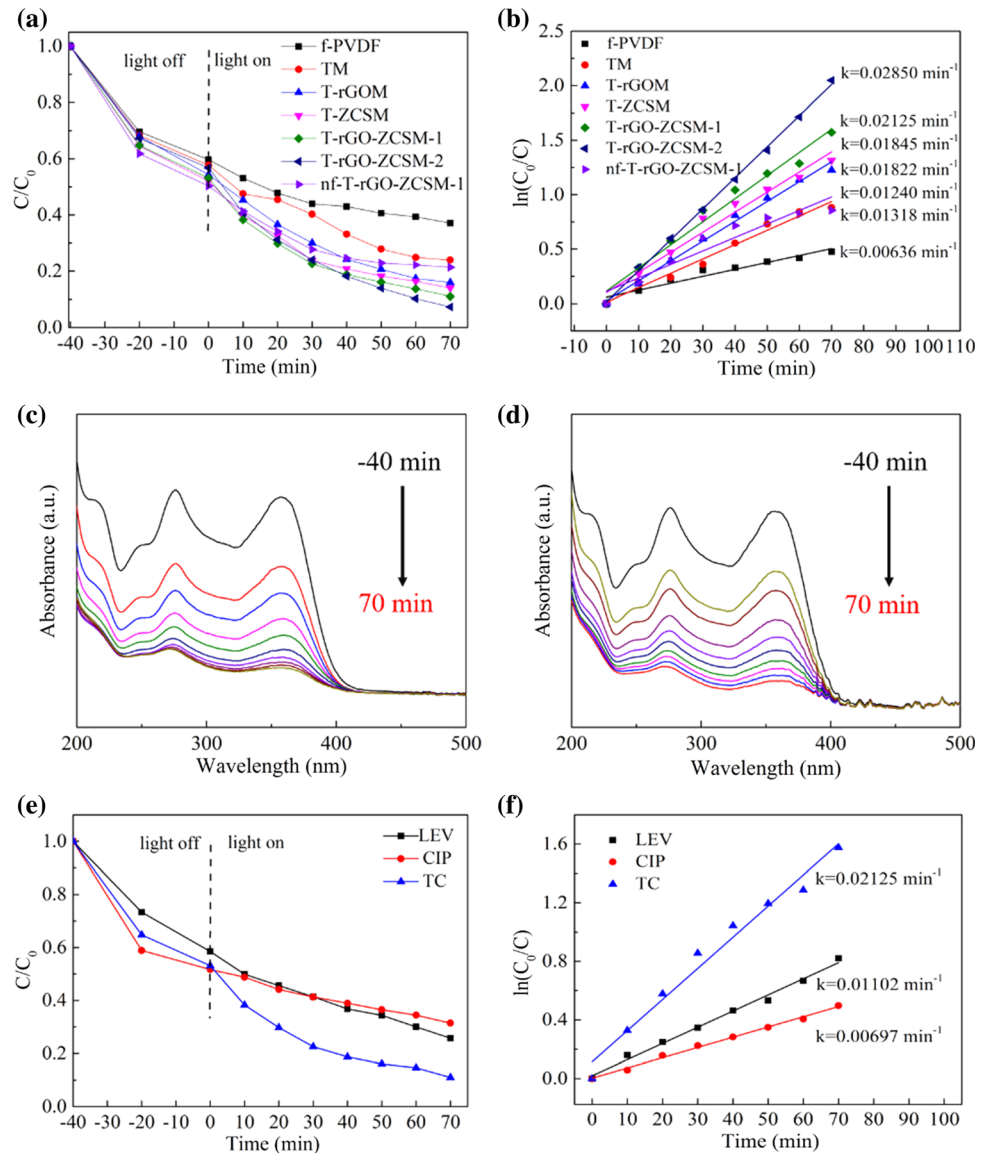
**Figure 7** The EDS mapping images of the top surface (a) and cross-section (b) of T-rGO-ZCSM-1 membrane.

according to the different color contrast of the picture, the top surface (a) and cross-sectional (b) EDS mapping images of a representative T-rGO-ZCSM-1 membrane exhibit the uniform distribution of C, O, F, Ti, Zn, Cd and S elements on the selection area of T-rGO-ZCSM-1 membrane.

Photocatalytic activity of membranes

With TC (20 mg/L), CIP (25 mg/L) and LEV (25 mg/L) as model pollutants, the photocatalytic performances of as-prepared membranes were investigated under visible light irradiation. The changes of TC, CIP and LEV concentration were measured in UV-Vis absorption spectra at 358, 276 and 287 nm,

Figure 8 **a** Effect of various membranes on the degradation of 100 mL TC (20 mg/L), absorbance variations of TC over **c** T-rGO-ZCSM-1 and **d** T-rGO-ZCSM-2. **e** Photocatalytic degradation of 100 mL TC (20 mg/L), CIP and LEV (25 mg/L) on the T-rGO-ZCSM-1. **b**, **f** The pseudo-first-order reaction kinetics. All the experiments were carried out under visible light irradiation.



respectively. The photocatalytic membranes and model pollutants for 40 min adsorption ability are monitored in the dark before visible light irradiation. As shown in Fig. 8, the results show that various membranes have strong adsorption capacity, which provides a prerequisite for visible light degradation. For the degradation process, it was found that the excellent photocatalytic activity of T-rGO-ZCSM was obtained. The degradation efficiency of T-rGO-ZCSM-1 and T-rGO-ZCSM-2 is higher than that of TM in 70 min, which is 2.16 times and 1.61 times that of TM, respectively (Fig. 8b). However, for T-rGO-ZCSM membranes with different catalyst contents, T-rGO-ZCSM-2 exhibits more prominent photocatalytic performance. This also shows that the

photocatalytic performance of a piece of membrane is affected by the content of the photocatalysts. Compared with non-freezing T-rGO-ZCSM-1 (nf-T-rGO-ZCSM-1) after 70 min irradiation, the photocatalytic activity of T-rGO-ZCSM-1 was significantly increased by 21.74%. This indicates that using the freezing phase inversion method to prepare the photocatalytic composite membrane with a macroporous structure is an effective method for the organic combination of photocatalysts and polymer to improve the photocatalytic performance. Among them, 37.90% of TC can be removed by the pure f-PVDF membrane, and these results can prove that the freezing PVDF membrane and photocatalysts can synergy and effectively improve the catalytic performance. In

addition, Fig. 8c, d directly reflects the absorption curve of TC under dark reaction and visible light, which confirms the fact that the as-prepared photocatalytic membrane degrades TC. It is worth noting that in Fig. 8e, f, the T-rGO-ZCSM-1 membrane also exhibits excellent photocatalytic performance when 25 mg/L of CIP and LEV was degraded. All the above degradation experiments show that the T-rGO-ZCSM photocatalytic composite membranes can effectively remove various organic pollutants under visible light. Therefore, T-rGO-ZCSM may hold broad application prospects in the field of photocatalytic composite membranes.

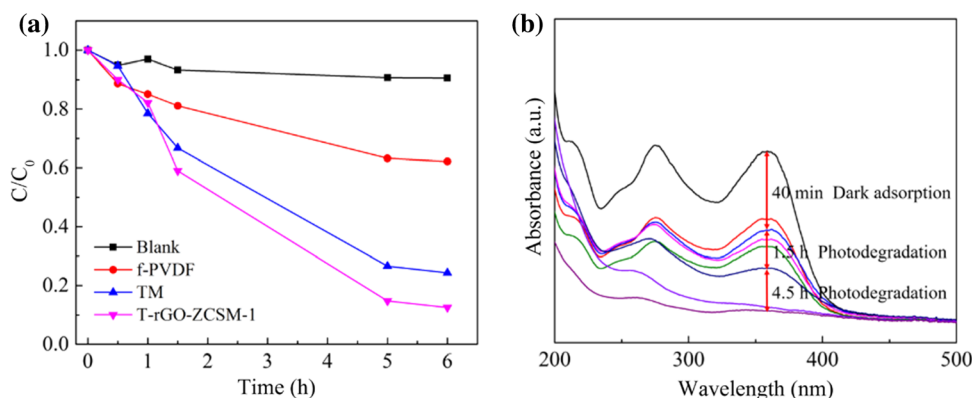
The practical application of photocatalytic composite membranes has great significance. Therefore, the photocatalytic characteristics of the T-rGO-ZCSM-1 membrane under solar light were discussed (Fig. 9a, b). Similarly, except for the light source, the same conditions as those under xenon lamp irradiation were adopted. After 6.0 h of outdoor solar exposure, the TC degradation rate of the T-rGO-ZCSM-1 membrane reached 87.46%. It shows that the T-rGO-ZCSM-1 membrane has the application potential of treating TC in actual wastewater under natural conditions. The “photocatalytic activity” of pure PVDF membrane and blank TC may be caused by membrane adsorption and self-photodegradation of TC under solar light. It is worth noting that the TC degradation efficiency of TM can also reach 75.65%. The photocatalytic degradation rates of TM and T-rGO-ZCSM-1 are relatively constant, indicating that the photocatalytic composite membranes remain stable, which is not only due to the excellent activity of photocatalysts, but also due to the excellent thermal stability, mechanical property (Fig. 10b) and chemical resistance of the PVDF, and the stable water permeability of the catalytic membrane. Moreover,

the excellent compatibility between photocatalysts and polymer membrane further solves the problem that catalyst particles are difficult to recover.

Permeability, mechanical properties, antifouling performance and reusability of membranes

The pure water permeation flux of the membranes is shown in Fig. 10a. All the freezing membranes revealed higher water permeation fluxes in comparison with non-freezing membranes. The pure water permeation flux of the freezing membranes can reach more than $19,000 \text{ L m}^{-2} \text{ h}^{-1} \text{ bar}^{-1}$. After a filtration time of 110 min, the pure water flux of the freezing membranes remained almost unchanged, which indicated that the membrane has good stability. The improvement of pure water flux may be due to the formation of macroporous and porous structures in the process of freezing phase inversion, which promotes the water permeability of the membranes under a certain pressure. According to the results of the mean pore radius given in Table 2, all freezing membranes show a larger mean pore radius than non-freezing membranes, which undoubtedly benefits water permeability. The membrane fouling characteristics were determined by a static BSA adsorption experiment (Fig. 10c). Compared with nf-T-rGO-ZCSM-1, T-rGO-ZCSM-1 showed lower BSA adsorption capacity. The BSA adsorption capacity significantly decreases T-rGO-ZCSM-2 with the increase in $\text{TiO}_2/\text{rGO}/\text{ZCS}$ -13% loading. This may be because the hydrophilicity of membranes affects the adsorption of BSA. In this way, it shows that the surface properties of T-rGO-ZCSM have been improved.

Figure 9 **a** Photocatalytic degradation efficiency of TC (100 mL, 20 mg/L) over PVDF, TM and T-rGO-ZCSM-1 under solar irradiation, **b** absorbance variations of TC over T-rGO-ZCSM-1.



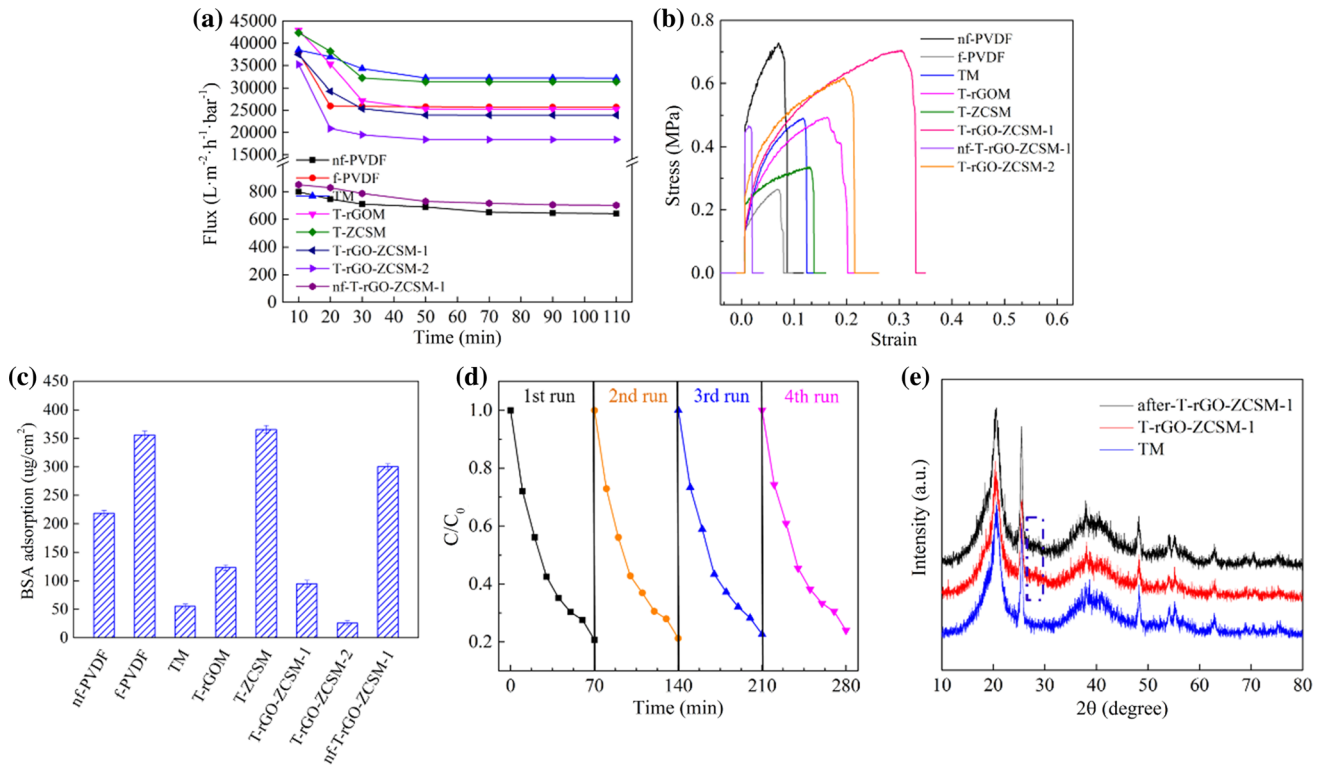


Figure 10 **a** The pure water flux, **b** the stress–strain curves and **c** static BSA adsorption capacity of membranes, **d** reusability of T-rGO-ZCSM-1 degradation TC (20 mg/L), **e** XRD patterns of T-rGO-ZCSM-1 before and after several reaction cycles.

The mechanical properties of the membranes were evaluated by testing the stress–strain curves. The good mechanical properties are one of the main factors determining the practical application of membranes. It can be seen from Fig. 10b that the f-PVDF membrane has a lower tensile strength at break compared with the nf-PVDF membrane. However, the tensile strength at break and the elongation at break of the T-rGO-ZCSM-1 were significantly increased compared with nf-T-rGO-ZCSM-1 and show the best mechanical properties, indicating that the embedment of TiO₂/rGO/ZCS-13% nanoparticles and freezing phase inversion can improve the mechanical strength of the membranes. For the 2 wt% TiO₂/rGO/ZCS-13% content, the tensile strength at break (from 0.71 to 0.61 MPa) and the elongation at break (from 33.14 to 21.57%) decrease slightly, and the results show that excessive TiO₂/rGO/ZCS-13% doped in PVDF matrix will weaken the mechanical strength of the membrane.

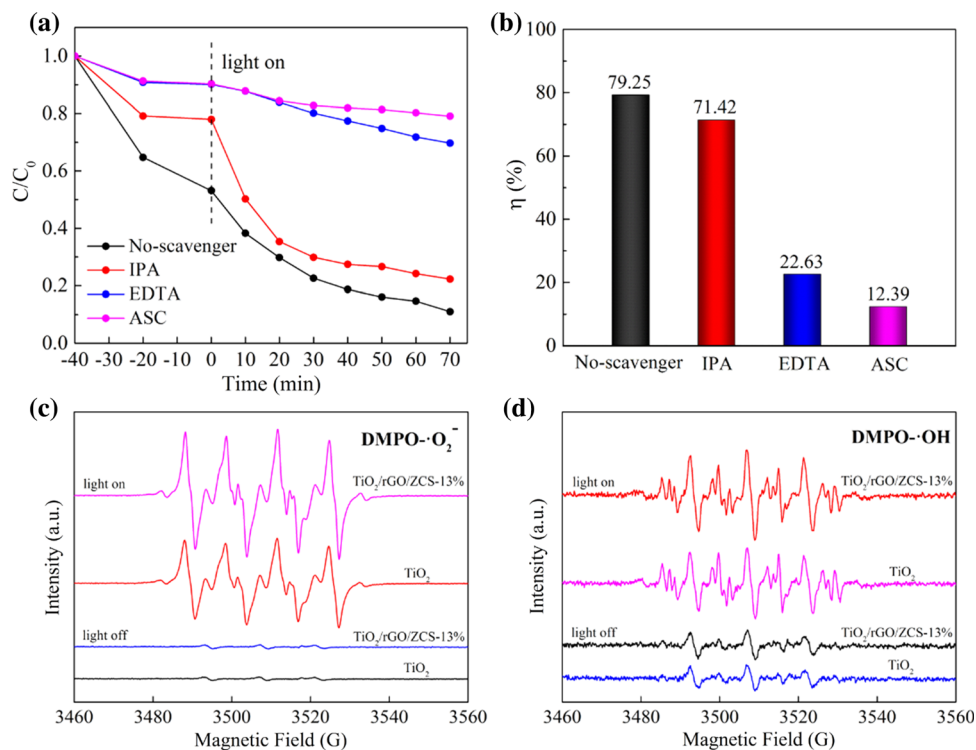
In addition, in order to test the photocatalytic stability of T-rGO-ZCSM-1, the cycle experiments of representative T-rGO-ZCSM-1 were studied. As shown in Fig. 10d, we can see clearly that the TC

degradation efficiency of T-rGO-ZCSM-1 decreased from 79.25 to 76.03% after four consecutive cycles under visible light irradiation, with only a slight change of 3.22%. The result indicates that T-rGO-ZCSM-1 has good degradation stability. For further study of the stability of the as-prepared T-rGO-ZCSM-1, we also analyzed the XRD spectra of the T-rGO-ZCSM-1 before and after four consecutive run experiments. The main characteristic diffraction peaks of T-rGO-ZCSM-1 has no apparent change from the before pattern after four consecutive cycles, which present the crystal structure is unchanged (Fig. 10e). Therefore, the T-rGO-ZCSM-1 possesses excellent photocatalyst recyclability and photocatalytic stability. These good properties make T-rGO-ZCSM very promising in actual wastewater treatment.

Photocatalytic mechanism of membrane

To better understand the possible degradation mechanism of the T-rGO-ZCSM membrane, the radicals trapping experiments were investigated by adding different trapping scavengers. The

Figure 11 a–b Photocatalytic degradation efficiency of TC (100 mL, 20 mg/L) using different scavengers over T-rGO-ZCSM-1 under visible light irradiation. DMPO spin-trapping ESR spectra for TiO_2 and $\text{TiO}_2/\text{rGO}/\text{ZCS-13\%}$: **c** in CH_3OH dispersion for $\text{DMPO}\cdot\text{O}_2^-$, **d** in H_2O dispersion for $\text{DMPO}\cdot\text{OH}$.



isopropanol (IPA), ethylenediaminetetraacetic acid disodium salt (EDTA-2Na) and ascorbic acid (ASC) were used as scavengers for hydroxyl ($\cdot\text{OH}$), holes (h^+) and superoxide ($\cdot\text{O}_2^-$), respectively. As shown in Fig. 11a, b, compared with no scavenger, the photocatalytic degradation efficiency (71.42%) of TC was slightly changed after the addition of IPA, indicating that $\cdot\text{OH}$ was not the main radicals during the degradation of TC. Oppositely, when EDTA-2Na and ASC were added, the photocatalytic degradation efficiency of TC was reduced to 22.63% and 12.39%, respectively. The photocatalytic degradation was greatly restrained, which also indicated that h^+ and $\cdot\text{O}_2^-$ were the main reactive species in the process of TC degradation.

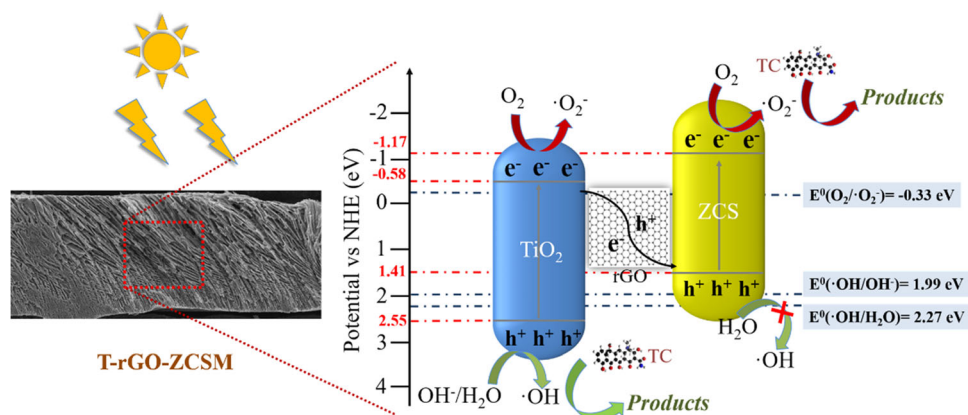
Additionally, for further evaluating the presence of $\cdot\text{O}_2^-$ and $\cdot\text{OH}$ radicals during the photocatalytic degradation process by T-rGO-ZCSM, the ESR trap technique was used to test. Figure 11c exhibits the $\text{DMPO}\cdot\text{O}_2^-$ characteristic peaks of TiO_2 and $\text{TiO}_2/\text{rGO}/\text{ZCS-13\%}$. No obvious ESR signals of pure TiO_2 and $\text{TiO}_2/\text{rGO}/\text{ZCS-13\%}$ were found in the dark. After visible light irradiation, the obvious characteristic signals of $\text{DMPO}\cdot\text{O}_2^-$ was observed in methanol suspension. At the same time, it is worth noting that compared with pure TiO_2 , $\text{TiO}_2/\text{rGO}/\text{ZCS-13\%}$ shows stronger signal intensity, which means that

more $\cdot\text{O}_2^-$ active species will be produced in photocatalytic degradation reaction. Similarly, we also studied the formation of $\text{DMPO}\cdot\text{OH}$ during degradation processes in aqueous suspension (Fig. 11d), and the weak $\cdot\text{OH}$ radical signals appeared in the dark, indicating that TiO_2 and $\text{TiO}_2/\text{rGO}/\text{ZCS-13\%}$ systems can produce $\cdot\text{OH}$ even without light irradiation. When irradiated by visible light, the signals of $\text{DMPO}\cdot\text{OH}$ were enhanced. Importantly, the ESR signal intensity of $\text{DMPO}\cdot\text{OH}$ is relatively weaker than that of $\text{DMPO}\cdot\text{O}_2^-$. Therefore, ESR and trapping experiments confirmed that $\cdot\text{O}_2^-$ is more important in the degradation of TC.

To further understand the photocatalytic mechanism of T-rGO-ZCSM and the migration trend of photogenerated carriers, we calculated the bandgap energy (E_g) (Fig. 1d) and XPS-VB (valence band) spectrum of pure TiO_2 and ZCS, and obtained the CB (conduction band) edge potential according to the empirical formula $E_{\text{VB}} = E_{\text{CB}} + E_g$. The experimental results show that the VB edge energy level distances of TiO_2 and ZCS are 2.55 and 1.41 eV (vs. NHE), respectively. The CB edge energy level distances are -0.58 and -1.17 eV (vs. NHE), respectively (Fig. S5b and c).

Based on the above experimental results and the photocatalytic mechanism reports, a possible reaction

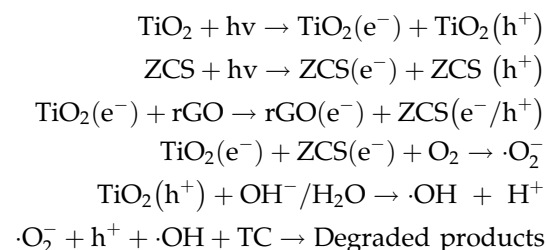
Figure 12 Schematic diagram of the TC photodegradation mechanism of T-rGO-ZCSM membranes.



mechanism of T-rGO-ZCSM was proposed and is displayed in Fig. 12. Under the solar light irradiation, the quantity of photogenerated carriers can be produced by Z-scheme $\text{TiO}_2/\text{rGO}/\text{ZCS}$ composite photocatalysts within the PVDF matrix. It can be clearly seen from the edge position of the catalyst conduction and valence bands that the CB values for TiO_2 and ZCS are more negative than $E^0(\text{O}_2/\cdot\text{O}_2^-)$ (-0.33 eV vs NHE), indicating that the photogenerated electrons can react with O_2 to generate more $\cdot\text{O}_2^-$, which is consistent with the results of radical trapping experiments and ESR technology. However, the redox potential of $E(\cdot\text{OH}/\text{H}_2\text{O})$ is 2.27 eV (vs NHE), and the h^+ in VB ($E_{\text{VB}} = 1.41$ eV vs NHE) of ZCS is not enough to oxidize H_2O to $\cdot\text{OH}$. Besides, the VB ($E_{\text{VB}} = 2.55$ eV vs NHE) position of TiO_2 is higher than $E(\cdot\text{OH}/\text{H}_2\text{O})$ and $E(\cdot\text{OH}/\text{OH}^-)$ (1.99 eV vs NHE), and the h^+ in VB of TiO_2 can react with $\text{OH}^-/\text{H}_2\text{O}$ to form $\cdot\text{OH}$, respectively [51]. Therefore, the Z-scheme photocatalytic mechanism is formed. Due to the introduction of rGO and the work function of -0.08 eV [52], the ladder structure of this energy level is conducive to the transfer of photogenerated electrons from TiO_2 to rGO and recombination with h^+ in the valence band of ZCS, rGO with high electron mobility not only provides a fast electron transport channel between TiO_2 and ZCS but also effectively inhibits the recombination of photogenerated electron–hole pairs to increase the number of active species, which is conducive to enhancing the photocatalytic performance of the photocatalytic composite membrane.

Owing to the functionality of the photocatalytic membrane, more TC molecules are adsorbed on its surface and pore channel and react with $\cdot\text{O}_2^-$, h^+ and $\cdot\text{OH}$. (Among them, $\cdot\text{OH}$ is not the main active

substance.) Therefore, possible photocatalytic reaction processes are described as follows:



Conclusions

In summary, firstly a novel Z-scheme $\text{TiO}_2/\text{rGO}/\text{ZCS}$ heterojunctions were prepared by hydrothermal method. Then, $\text{TiO}_2/\text{rGO}/\text{ZCS}$ composite photocatalysts were blended into PVDF matrix, and the T-rGO-ZCSM photocatalytic composite membranes with a high-performance micron-scale size ordered penetrating-type macroporous structure were successfully prepared by freezing phase inversion method. The prepared T-rGO-ZCSM photocatalytic composite membranes displayed outstanding photocatalytic performance in the degradation of TC, LEV, and CIP under visible light irradiation, and the TC degradation efficiency was 1.61 times and 1.71 times higher than that of TM and non-freezing nf-T-rGO-ZCSM-1, respectively. Importantly, the membrane also exhibits excellent photodegradation ability (87.46%) under solar light. After T-rGO-ZCSM degraded TC for four cycles, it still showed obvious photocatalytic performance and good stability. Meanwhile, the T-rGO-ZCSM exhibited ultra-high-pure water flux, excellent mechanical properties and better self-cleaning performance compared to nf-

PVDF and nf-T-rGO-ZCSM-1. The freezing T-rGO-ZCSM photocatalytic composite membranes prepared in this work has great potential to treat antibiotics in wastewater under solar light irradiation.

Acknowledgements

We gratefully acknowledge the financial support from the National Natural Science Foundation of China (No. 21806060, 21808089 and 21776110), the Postgraduate Research & Practice Innovation Program of Jiangsu Province (No. KYCX19_1589) and the Natural Science Foundation of Jiangsu Province (BK20181230, BK20180192, BK20190245).

Declarations

Conflict of interest The authors declare that they have no known competing financial interests or personal relationships that could have appeared to influence the work reported in this paper.

Supplementary Information: The online version contains supplementary material available at <http://doi.org/10.1007/s10853-021-06438-4>.

References

- [1] Cui Y, Yang L, Meng M, Zhang Q, Li B, Wu Y, Zhang Y, Lang J, Li C (2019) Facile preparation of antifouling g-C₃N₄/Ag₃PO₄ nanocomposite photocatalytic polyvinylidene fluoride membranes for effective removal of rhodamine B. *Korean J Chem Eng* 36:236–247
- [2] Li B, Guo Z, Feng Y, Meng M (2021) A multi-functional photothermal-catalytic foam for cascade treatment of saline wastewater. *J Mater Chem A*
- [3] Li B, Wang H, Lan Y, Cui Y, Zhang Y, Feng Y, Pan J, Meng M, Wu C (2020) A controllable floating pDA-PVDF bead for enhanced decomposition of H₂O₂ and degradation of dyes. *Chem Eng J* 385:123907
- [4] Li J, Ma Y, Ye Z, Zhou M, Wang H, Ma C, Wang D, Huo P, Yan Y (2017) Fast electron transfer and enhanced visible light photocatalytic activity using multi-dimensional components of carbon quantum dots@3D daisy-like In₂S₃/single-wall carbon nanotubes. *Appl Catal B* 204:224–238
- [5] Li J, Liu K, Xue J, Xue G, Sheng X, Wang H, Huo P, Yan Y (2019) CQDs preluded carbon-incorporated 3D burger-like hybrid ZnO enhanced visible-light-driven photocatalytic activity and mechanism implication. *J Catal* 369:450–461
- [6] Li B, Meng M, Cui Y, Wu Y, Zhang Y, Dong H, Zhu Z, Feng Y, Wu C (2019) Changing conventional blending photocatalytic membranes (BPMs): focus on improving photocatalytic performance of Fe₃O₄/g-C₃N₄/PVDF membranes through magnetically induced freezing casting method. *Chem Eng J* 365:405–414
- [7] Zhu Z, Tang X, Fan W, Liu Z, Huo P, Wang T, Yan Y, Li C (2019) Studying of Co-doped g-C₃N₄ and modified with Fe₃O₄ quantum dots on removing tetracycline. *J Alloys Compd* 775:248–258
- [8] Marcelino RBP, Leao MMD, Lago RM, Amorim CC (2017) Multistage ozone and biological treatment system for real wastewater containing antibiotics. *J Environ Manag* 195:110–116
- [9] Yu K, Sun C, Zhang B, Hassan M, He Y (2019) Size-dependent adsorption of antibiotics onto nanoparticles in a field-scale wastewater treatment plant. *Environ Pollut* 248:1079–1087
- [10] Alves AMB, Morao A, Cardoso JP (2002) Isolation of antibiotics from industrial fermentation broths using membrane technology. *Desalination* 148:181–186
- [11] Zhu X, Yang J, She X, Song Y, Qian J, Wang Y, Xu H, Li H, Yan Q (2019) Rapid synthesis of ultrathin 2D materials through liquid-nitrogen and microwave treatments. *J Mater Chem A* 7(10):5209–5213
- [12] Gao X, Ma C, Liu Y, Xing L, Yan Y (2019) Self-induced Fenton reaction constructed by Fe(III) grafted BiVO₄ nanosheets with improved photocatalytic performance and mechanism insight. *Appl Surf Sci* 467:673–683
- [13] Sun L, Li J, Li X, Liu C, Wang H, Huo P, Yan Y (2019) Molecularly imprinted Ag/Ag₃VO₄/g-C₃N₄ Z-scheme photocatalysts for enhanced preferential removal of tetracycline. *J Colloid Interface Sci* 552:271–286
- [14] Babic S, Curkovic L, Ljubas D, Cizmi M (2017) TiO₂ assisted photocatalytic degradation of macrolide antibiotics. *Curr Opin Green Sust* 6:34–41
- [15] Dong S, Cui L, Zhang W, Xia L, Zhou S, Russell CK, Fan M, Feng J, Sun J (2020) Double-shelled ZnSnO₃ hollow cubes for efficient photocatalytic degradation of antibiotic wastewater. *Chem Eng J* 384:123279
- [16] Yan W, Yan L, Jing C (2019) Impact of doped metals on urea-derived g-C₃N₄ for photocatalytic degradation of antibiotics: Structure, photoactivity and degradation mechanisms. *Appl Catal B* 244:475–485
- [17] Zhu X, Yang J, Zhu X, Yuan J, Zhou M, She X, Yu Q, Song Y, She Y, Hua Y, Li H, Xu H (2021) Exploring deep effects of atomic vacancies on activating CO₂ photoreduction via

- rationally designing indium oxide photocatalysts. *Chem Eng J* 422:129888
- [18] Li H, Wang D, Fan H, Wang P, Jiang T, Xie T (2011) Synthesis of highly efficient C-doped TiO₂ photocatalyst and its photo-generated charge-transfer properties. *J Colloid Interface Sci* 354:175–180
- [19] Tian J, Sang Y, Zhao Z, Zhou W, Wang D, Kang X, Liu H, Wang J, Chen S, Cai H, Huang H (2013) Enhanced photocatalytic performances of CeO₂/TiO₂ nanobelt heterostructures. *Small* 9:3864–3872
- [20] Xu F, Zhang J, Zhu B, Yu J, Xu J (2018) CuInS₂ sensitized TiO₂ hybrid nanofibers for improved photocatalytic CO₂ reduction. *Appl Catal B* 230:194–202
- [21] Kumar A, Sharma SK, Sharma G, AaH A-M, Naushad M, Ghfar AA, Stadler FJ (2019) Wide spectral degradation of Norfloxacin by Ag@BiPO₄/BiOBr/BiFeO₃ nano-assembly: elucidating the photocatalytic mechanism under different light sources. *J Hazard Mater* 364:429–440
- [22] Cao Y, Xing Z, Li Z, Wu X, Hu M, Yan X, Zhu Q, Yang S, Zhou W (2018) Mesoporous black TiO_(2-x)/Ag nanospheres coupled with g-C₃N₄ nanosheets as 3D/2D ternary heterojunctions visible light photocatalysts. *J Hazard Mater* 343:181–190
- [23] Li Y, Fang Y, Cao Z, Li N, Chen D, Xu Q, Lu J (2019) Construction of g-C₃N₄/PDI@MOF heterojunctions for the highly efficient visible light-driven degradation of pharmaceutical and phenolic micropollutants. *Appl Catal B* 250:150–162
- [24] Liu H, Jin Z, Xu Z (2015) Hybridization of Cd_{0.2}Zn_{0.8}S with g-C₃N₄ nanosheets: a visible-light-driven photocatalyst for H₂ evolution from water and degradation of organic pollutants. *Dalton Trans* 44:14368–14375
- [25] Chen J, Chen J, Li Y (2017) Hollow ZnCdS dodecahedral cages for highly efficient visible-light-driven hydrogen generation. *J Mater Chem A* 5:24116–24125
- [26] Li W, Li D, Chen Z, Huang H, Sun M, He Y, Fu X (2008) High-efficient degradation of dyes by Zn_xCd_{1-x}S solid solutions under visible light irradiation. *J Phys Chem C* 112:14943–14947
- [27] Qi S, Wang D, Zhao Y, Xu H (2019) Core-shell g-C₃N₄@Zn_{0.5}Cd_{0.5}S heterojunction photocatalysts with high photocatalytic activity for the degradation of organic dyes. *J Mater Sci Mater Electron* 30:5284–5296
- [28] Song L, Liu D, Zhang S, Wei J (2019) WO₃ cocatalyst improves hydrogen evolution capacity of ZnCdS under visible light irradiation. *Int J Hydrogen Energy* 44:16327–16335
- [29] Zhang J, Yu J, Jaroniec M, Gong JR (2012) Noble metal-free reduced graphene oxide-ZnxCd1-xS nanocomposite with enhanced solar photocatalytic H₂-production performance. *Nano Lett* 12:4584–4589
- [30] Wu F, Li X, Liu W, Zhang S (2017) Highly enhanced photocatalytic degradation of methylene blue over the indirect all-solid-state Z-scheme g-C₃N₄-RGO-TiO₂ nanoheterojunctions. *Appl Surf Sci* 405:60–70
- [31] Pawar RC, Khare V, Lee CS (2014) Hybrid photocatalysts using graphitic carbon nitride/cadmium sulfide/reduced graphene oxide (g-C₃N₄/CdS/RGO) for superior photodegradation of organic pollutants under UV and visible light. *Dalton Trans* 43:12514–12527
- [32] Xiao Y, Zhang W, Jiao Y, Xu Y, Lin H (2021) Metal-phenolic network as precursor for fabrication of metal-organic framework (MOF) nanofiltration membrane for efficient desalination. *J Membr Sci* 624:119101
- [33] Leong SW, Razmjou A, Wang K, Hapgood K, Zhang XW, Wang HT (2014) TiO₂ based photocatalytic membranes: a review. *J Membr Sci* 472:167–184
- [34] Li R, Rao L, Zhang J, Shen L, Xu Y, You X, Liao B-Q, Lin H (2021) Novel in-situ electroflotation driven by hydrogen evolution reaction (HER) with polypyrrole (PPy)-Ni-modified fabric membrane for efficient oil/water separation. *J Membr Sci* 635:119502
- [35] Shi Y, Huang J, Zeng G, Cheng W, Hu J (2019) Photocatalytic membrane in water purification: is it stepping closer to be driven by visible light? *J Membr Sci* 584:364–392
- [36] Yang F, Ding G, Wang J, Liang Z, Gao B, Dou M, Xu C, Li S (2020) Self-cleaning, antimicrobial, and antifouling membrane via integrating mesoporous graphitic carbon nitride into polyvinylidene fluoride. *J Membr Sci* 606:118146
- [37] Yu S, Wang Y, Sun F, Wang R, Zhou Y (2018) Novel mpg-C₃N₄/TiO₂ nanocomposite photocatalytic membrane reactor for sulfamethoxazole photodegradation. *Chem Eng J* 337:183–192
- [38] Zhou S, Gao J, Zhu J, Peng D, Zhang Y, Zhang Y (2020) Self-cleaning, antibacterial mixed matrix membranes enabled by photocatalyst Ti-MOFs for efficient dye removal. *J Membr Sci* 610:118219
- [39] You X, Zhang J, Shen L, Li R, Xu Y, Zhang M, Hong H, Yang L, Ma Y, Lin H (2021) Thermodynamic mechanisms of membrane fouling during filtration of alginate solution in coagulation-ultrafiltration (UF) process in presence of different ionic strength and iron(III) ion concentration. *J Membr Sci* 635:119532
- [40] Long Y, Yu G, Dong L, Xu Y, Lin H, Deng Y, You X, Yang L, Liao B-Q (2021) Synergistic fouling behaviors and mechanisms of calcium ions and polyaluminum chloride associated with alginate solution in coagulation-ultrafiltration (UF) process. *Water Res* 189:116665

- [41] Lu J, Qin Y, Zhang Q, Yu C, Wu Y, Yan Y, Fan H, Meng M, Li C (2019) Antibacterial, high-flux and 3D porous molecularly imprinted nanocomposite sponge membranes for cross-flow filtration of emodin from analogues. *Chem Eng J* 360:483–493
- [42] Gu J, Gu H, Zhang Q, Zhao Y, Li N, Xiong J (2018) Sandwich-structured composite fibrous membranes with tunable porous structure for waterproof, breathable, and oil-water separation applications. *J Colloid Interface Sci* 514:386–395
- [43] Thankamony RL, Li X, Fan XL, Sheng G, Wang XB, Sun SY, Zhang XX, Lai ZP (2018) Preparation of highly porous polymer membranes with hierarchical porous structures via spinodal decomposition of mixed solvents with UCST phase behavior. *ACS Appl Mater Interfaces* 10:44041–44049
- [44] Mohamed M, Dayirou N, Mohamed H, Andre N, Laure D, Daniels N (2020) Effect of porogenic agent type and firing temperatures on properties of low-cost microfiltration membranes from Kaolin. *Trans Indian Ceram Soc* 79:1–12
- [45] Zhang H, Hussain I, Brust M, Butler MF, Rannard SP, Cooper AI (2005) Aligned two- and three-dimensional structures by directional freezing of polymers and nanoparticles. *Nat Mater* 4:787–793
- [46] Fu J, Zhu B, You W, Jaroniec M, Yu J (2018) A flexible bio-inspired H₂-production photocatalyst. *Appl Catal B* 220:148–160
- [47] Li Z, Wnetrzak R, Kwapinski W, Leahy JJ (2012) Synthesis and characterization of sulfated TiO₂ nanorods and ZrO₂/TiO₂ nanocomposites for the esterification of biobased organic acid. *ACS Appl Mater Interfaces* 4:4499–4505
- [48] Luo Z, Zhao X, Zhang H, Jiang Y (2019) Zn_{0.3}Cd_{0.7}S nanorods loaded with noble-metal-free Ni₃C co-catalyst enhancing photocatalytic hydrogen evolution. *Appl Catal A* 582:117115
- [49] Dai B, Huang H, Wang F, Lu C, Kou J, Wang L, Xu Z (2018) Flowing water enabled piezoelectric potential of flexible composite film for enhanced photocatalytic performance. *Chem Eng J* 347:263–272
- [50] Xie A, Cui J, Yang J, Chen Y, Lang J, Li C, Yan Y, Dai J (2020) Photo-Fenton self-cleaning PVDF/NH₂-MIL-88B(Fe) membranes towards highly-efficient oil/water emulsion separation. *J Membr Sci* 595:117499
- [51] Kumar A, Sharma G, Naushad M, Ahamad T, Veses RC, Stadler FJ (2019) Highly visible active Ag₂CrO₄/Ag/BiFeO₃@RGO nano-junction for photoreduction of CO₂ and photocatalytic removal of ciprofloxacin and bromate ions: the triggering effect of Ag and RGO. *Chem Eng J* 370:148–165
- [52] Xiang Q, Yu J, Jaroniec M (2011) Enhanced photocatalytic H₂-production activity of graphene-modified titania nanosheets. *Nanoscale* 3:3670–3678

Publisher's Note Springer Nature remains neutral with regard to jurisdictional claims in published maps and institutional affiliations.